

Constraints on the energetics and plasma composition of relativistic jets in FR II sources

Motoki Kino^{1,2} and Fumio Takahara²

¹ Department of Earth and Planetary Science, University of Tokyo, Tokyo 113-0033, Japan

² Department of Earth and Space Science, Osaka University, Toyonaka 560-0043, Japan

submitted to MNRAS 2003 March 28

ABSTRACT

We explore the energetics and plasma composition in FR II sources using a new simple method of combining shock dynamics and radiation spectrum. The hot spots are identified with the reverse shocked region of jets. With the one-dimensional shock jump conditions taking account of the finite pressure of hot ICM, we estimate the rest mass and energy densities of the sum of thermal and non-thermal particles in hot spots. Independently, based on the Synchrotron Self-Compton (SSC) model, we estimate the number and energy densities of *non-thermal* electrons using the multi-frequency radiation spectrum of hot spots. We impose the condition that the obtained rest mass, internal energy, and number densities of non-thermal electrons should be lower than those of the total particles determined by shock dynamics. We apply this method to Cygnus A. We examine three extreme cases of pure electron-positron pair plasma (Case I), pure electron-proton plasma with separate thermalization (Case II), and pure electron-proton plasma in thermal-equilibrium (Case III). By detailed SSC analysis for Cygnus A and 3C123, we find that the energy density of non-thermal electrons is about 10 times larger than that of magnetic field. We find that the Case III is not acceptable because predicted photon spectra do not give a good fit to the observed one. We find that Case II can also be ruled out since the number density of non-thermal electrons exceeds that of the total number density. Hence, we find that only pure e^\pm plasma (Case I) is acceptable among the three cases. Total kinetic power of jet and electron acceleration efficiency are also constrained by internal energy densities of non-thermal and total particles.

Key words: Radio Galaxies: general—shocks: theory—radiation mechanisms: non-thermal

1 INTRODUCTION

Energetics and plasma composition of relativistic jets in active galactic nuclei (AGN) is one of the unresolved issues for understanding the jet physics. Recently, *Chandra X-ray Observatory* has detected inverse Compton X-rays from hot spots in FR II sources (e.g., Harris et al. 2000; Wilson, Young & Shopbell 2000; Hardcastle, Birkinshaw, & Worrall 2001; Hardcastle et al. 2002). We can now remove the degeneracy between the energy density of relativistic electrons and magnetic field by using both the inverse Compton component and the synchrotron component.

Since these photons are produced by shock-accelerated electrons, the existence of thermal particles which drive the shocks is not directly probed. In this paper, we will explore the physical quantities of thermal plasma by using the shock dynamics. It is clear that both thermal and non-thermal plasma contribute to the dynamical processes in hot spots.

Many authors have studied the dynamics of cocoon using both analytical and numerical approaches (e.g., Begelman & Cioffi 1989; Falle 1991; Kaiser & Alexander 1997; Smith et al. 1985; Scheck et al. 2002). However, little has been discussed about the energy and number density ratio of the shock-accelerated electrons to the total particles (thermal plus non-thermal) and the issue of electron acceleration efficiency is still open up to now. If the energy density of accelerated particles is negligible compared to that of thermal particles, it means that there is a large amount of missing kinetic power of thermal particles. Furthermore, quantitative study of missing power will give some constraints on the problem of plasma composition.

In order to explore these issues, in §2, we outline the method to constrain the energetics and plasma contents by comparing the rest mass and energy densities of shock accelerated electrons and total particles obtained by the analysis

of shock dynamics. Here we include the issue of shock jump conditions. In §3, we investigate the energetics of shock accelerated electrons, magnetic field and radiation field in hot spot of Cygnus A and 3C123 based on observed non-thermal radiation spectra. We apply the method developed in §2 to Cygnus A. We summarize our conclusions of constraints on energetics and plasma composition of FR II sources in §4.

2 GENERAL CONSIDERATION

It is widely accepted that shock waves accelerate *some fraction* of the electrons and protons in the shocked region and then shock accelerated (relativistic) electrons produce the observed non-thermal emission. It is worth emphasizing that by definition, physical quantities of shock accelerated particles never exceed those of total particles. Based on this key point, the aim of this paper is to constrain the energetics and plasma contents.

To this end, here we will investigate the number and energy densities of total particles in the shocked regions (see Figure 1) using the simple shock jump conditions with the aid of observed ICM physical quantities and advance speed of hot spots. By comparing the number and energy densities of relativistic electrons and total particles (we will explore the number and energy densities of the shock accelerated electrons in the emission region of hot spots in the next section), we give constraints on the energetics and plasma contents.

2.1 Shock Dynamics Applied to the Hot Spots

Here we discuss the dynamics of shocks at the head of jets. Let us consider the dynamics of an AGN jet which impinges into a hot Intra-Cluster Medium (ICM). Figure 1 shows the schematic view of interaction between the AGN jet and ICM. We know that two shocks form: the forward shock that propagates into the ICM and the reverse shock that propagates into the jet. A contact discontinuity separates the shocked jet and the shocked ICM.

2.1.1 Basic Assumptions

In order to grasp the essence of shock structure of AGN jets, we make several assumptions: (1) we use the 1D shock jump conditions, (2) we regard the forward shock as a non-relativistic one since the advance speed of hot spots is estimated to be in the range $0.01c$ to $0.1c$ (e.g., Liu, Pooley & Riley 1992; however see also Georganopoulos & Kazanas 2003), and adopt the adiabatic index of equation of state as $5/3$, (3) we assume the reverse shock as a relativistic one although the jet speed on Mpc scales is still open. Some are suggested to be relativistic (e.g., Tavecchio et al. 2000), (4) we assume that the magnetic fields are passive and ignore their dynamical effects, and, (5) we treat only one-component plasma compositions (i.e., pure e^\pm or pure ep) for simplicity. The validity of the assumption (1) is discussed at the end of this section.

2.1.2 Shock Jump Conditions

As shown in Fig. 1, we use the terminology of *region i* ($i=1, 2, 3$, and 4) with the number labeling the four regions in the head part of AGN jet as follows: (1) the unshocked ICM, (2) the shocked ICM, (3) the shocked jet which is identified with hot spots, and (4) the unshocked jet. Fluid velocity and Lorentz factor in the region i measured in the ICM rest frame are expressed as $v_i = \beta_i c$, and Γ_i , respectively. Relative velocity and relative Lorentz factor between the region i and j (velocity of region i measured from region j) are expressed as $v_{ij} = -v_{ji} = \beta_{ij} c = -\beta_{ji} c$, and $\Gamma_{ij} = \Gamma_{ji}$, respectively. As for the position of the forward shock front (FS), the contact discontinuity (CD), and reverse one (RS), we use the same labeling ($i=FS$, CD, and RS). Each region is characterized by three physical quantities; the rest mass density ρ_i , the pressure P_i , and the velocity v_i . In order to make the argument independent of the plasma composition of jets, we use the rest mass density rather than the number density. In the next subsection, we will discuss the issue of number density by specifying the composition as pure e^\pm or ep plasma.

Within the framework of 1D planar shock, pressure and velocity are uniform in each shocked region. Then, along the CD, we have velocity and pressure balance as, $v_2 = v_3$ and $P_2 = P_3$. In general, we can solve for $3 + 3 = 6$ physical quantities ρ_2 , $P_2 = P_3$, $v_2 = v_3$, ρ_3 , v_{FS} , and v_{RS} , when $3 + 3 = 6$ upstream quantities such as ρ_1 , P_1 , v_1 , ρ_4 , P_4 , and v_4 are given. In the case of the shock conditions of actual FR II sources, it is convenient to choose 6 givens in a different way. The properties of ICM (upstream) are known from X-ray observations to give $P_1 = P_{ICM}$, $\rho_1 = \rho_{ICM}$, and $v_1 = 0$. The hot spot (downstream) advance speed v_{HS} is inferred from observations. We regard that the unshocked jet is cold and $P_4 = 0$. Although there are some amount of relativistic electrons in the jet, observations and numerical simulations suggest that the internal Mach number of Cygnus A jet should be high (Carilli & Barthel 1996). Furthermore, to obtain a conspicuous hot spot identified with a strong shock, dynamically cold jet matter is the most natural choice. We adopt Γ_4 as a free parameter. To sum up, for actual FR II source, we regard that (1) $v_2 = v_3 = v_{HS}$ is given (observable) and that (2) ρ_4 can be solved. Then, by using the plausible shock conditions, we can obtain ρ_2 , $P_2 = P_3$, v_{FS} , ρ_3 , v_{RS} , and ρ_4 , as functions of Γ_4 .

Using the well-known shock jump conditions in non-relativistic limit (Landau & Lifshitz 1959), the forward shocked region quantities are given as

$$v_{FS} = \frac{2}{3} \left[v_{HS} + \sqrt{v_{HS}^2 + \frac{15}{4} \frac{P_1}{\rho_1}} \right], \quad (1)$$

$$\rho_2 = \frac{4}{1 + (3/\mathcal{M}_1^2)} \rho_1, \quad (2)$$

$$P_2 = \left[\frac{3 - (3/5\mathcal{M}_1^2)}{4} \right] \rho_1 v_{FS}^2, \quad (3)$$

where $\mathcal{M}_1 = v_{FS} / \sqrt{(5P_1/3\rho_1)}$ is the Mach number of the FS. In the reverse shocked region, by using the strong limit jump condition (Landau & Lifshitz 1959; Blandford & Mc-

Kee 1976) we have

$$\Gamma_{4RS}^2 = \frac{(\Gamma_{43} + 1)[\hat{\gamma}_3(\Gamma_{43} - 1) + 1]^2}{\hat{\gamma}_3(2 - \hat{\gamma}_3)(\Gamma_{43} - 1) + 2}, \quad (4)$$

$$\rho_3 = \left(\frac{\hat{\gamma}_3\Gamma_{43} + 1}{\hat{\gamma}_3 - 1} \right) \rho_4, \quad (5)$$

$$P_3 = (\hat{\gamma}_3 - 1)(\Gamma_{43} - 1)\rho_3 c^2, \quad (6)$$

where $\Gamma_{43} = \Gamma_3\Gamma_4(1 - \beta_3\beta_4) \simeq \Gamma_4$. By using the last remaining equation of pressure balance $P_2 = P_3$ with $\hat{\gamma}_3 = 4/3$, we can obtain ρ_4 as

$$\rho_4 = \frac{9}{20} \frac{5\mathcal{M}_1^2 - 1}{\mathcal{M}_1^2} \frac{1}{(\Gamma_{43} - 1)(4\Gamma_{43} + 3)} \rho_1 \beta_{FS}^2. \quad (7)$$

In order to discuss the physical condition of jets, it is convenient to introduce the dimensionless parameter

$$f \equiv \frac{\rho_4}{\rho_1} = \frac{9}{20} \frac{5\mathcal{M}_1^2 - 1}{\mathcal{M}_1^2} \frac{\beta_{FS}^2}{(\Gamma_{43} - 1)(4\Gamma_{43} + 3)}. \quad (8)$$

Conventionally we call a jet *light* for $f < 1$, and *heavy* for $f > 1$.

2.1.3 Sideway Expansion

Most of the hot spot models suppose that the heated plasma expands sideway (laterally) to supply the matter in the cocoon. Hence, let us discuss the role of sideway expansion (escape).

First, we consider what would occur if there is no lateral escape. The shock jump conditions shown above do not include any information on the longitudinal size of shocked region l_3 (see Fig. 1). Although little attention has been paid on l_3 , this strongly reflects a difference between the cases of escape and no escape. First, let us show a simple estimate of β_{3RS} as a preparation for the estimate of l_3 . A jet with relativistic speed of Γ_4 decelerates to sufficiently non-relativistic speed at the reverse shock, then we have $\beta_{4RS} \sim 1$. Besides, it is well known that, for a strong shock in a relativistic gas in which $\hat{\gamma}_3 = 4/3$, one has the relation of $\beta_{3RS} \times \beta_{4RS} = 1/3$ (e.g., Kirk & Duffy 1999). Therefore we have $\beta_{3RS} \sim 1/3$. Next, by exactly solving the β_{3RS} by using the relation of $\beta_{3RS} = (\beta_{34} - \beta_{RS4})/(1 - \beta_{RS4}\beta_{34})$, $0.01 < \beta_3 < 0.1$, and Eq. (4), we obtain the value of β_{3RS} is about 0.2–0.3. From this, we see that accuracy of the simple estimation of $\beta_{3RS} \sim 1/3$ is good enough. As for a timescale, we take the age of Cygnus A as $t_{age} \sim 10^7$ yr (Carilli et al. 1998). Then, the scale length of reverse shocked region $l_3 = t_{age} v_{3RS}$ is predicted to be order of Mpc, which definitely contradicts with the observed size. The reason for this is simply because we do not take the sideway escape effect into account.

Next, let us consider the case of including the escape effect. In reality, the shocked region expands laterally, too, which reduces l_3 significantly. The actual difference will appear in the size of the shocked region. In order to get more realistic value of l_3 , we may use t_{esc} which expresses the effective escaping timescale of shocked plasma from the hot spot, because shock accelerated particles do not stay in the hot spot during the whole lifetime but escape sideway. Then, we must evaluate as

$$l_3 \sim t_{esc} v_{3RS} \quad (9)$$

where t_{esc} is the effective escape time and we believe that this is identified as expansion time scale of shocked matter. This time scale is estimated by $t_{esc} \sim \frac{R_{HS}}{v_{esc}}$ where R_{HS} is the hot spot size perpendicular to the jet axis and v_{esc} is the mean escape velocity of shocked matter. If we take l_3 as observed size of the hot spot R_{HS} , this leads to v_{esc} of a few ten percent of the light speed and shocked plasma remains in the spot for only $t_{esc} \sim 1/1000t_{age} \sim 10^4$ yr. This picture is matched with the basic concept of synchrotron aging model (e.g., Carilli et al 1991) for hot spots. Our next concern is the escape velocity. Here we treat the time scale much longer than t_{esc} , for the system to be steady. The steady state requires that escaping amount of mass and energy from a shocked region is the same as those newly injected plasma in the region. In this case, the important point is that the jump conditions remain the same as pure 1D case. Conservation equations of mass and energy in the sideway direction correspond to determine the scale length (surface area) of the shocked region and the greatly simplified injection and escape balance relations are

$$\begin{aligned} R_{HS}^2 \rho_3 v_{3RS} &\sim R_{HS} l_3 \rho_3 v_{esc}, \\ R_{HS}^2 U_3 v_{3RS} &\sim R_{HS} l_3 U_3 v_{esc} \end{aligned} \quad (10)$$

where U_3 is the internal energy density in region 3. An obvious but not a unique estimate is $l_3 \sim R_{HS}$ and $v_{esc} \sim v_{3RS}$. To sum up, on the time scale of order t_{age} , the system can be regarded as steady and we expect that it evolves so as to keep the pressure and velocity constant and a series of the shock jump conditions in the present work remain the same ones. Hence we conclude that our 1D treatment well describes the shock dynamics of FR II sources because the shocked plasma escapes in a short time scale.

On the timescale close to t_{esc} , the study of 2D numerical simulation is required to assess the deviation of our simple analysis from more detailed hydrodynamical perspective.

2.2 Electron Acceleration Efficiency

Here we introduce two important quantities: the ratio of mass density of accelerated electrons to that of shocked jet (i.e. total particle mass density in the shocked jet) is defined as ζ and given by

$$\zeta \equiv \frac{\rho_{3,acc}}{\rho_3}, \quad (11)$$

and the ratio of internal energy density of accelerated electrons to total one of shocked jet is defined as ϵ and given by

$$\epsilon \equiv \frac{U_{3,acc}}{U_3} = \frac{(<\gamma> - 1)\rho_{3,acc}}{(\Gamma_{43} - 1)\rho_3}, \quad (12)$$

where $\rho_{3,acc}$ and $<\gamma>$ are the mass density and average Lorentz factor of shock-accelerated electrons, respectively. The determination of the shock-accelerated electrons is shown in the next section.

2.3 Physical Constraints

Let us discuss how to give constraints on the energetics and plasma composition. To begin with, we estimate the minimum Lorentz factor γ_{min} from which value an injection process occurs. The determination of γ_{min} is one of

the most important issues and it has been discussed from various points of view (e.g., Reynolds, Fabian, Celotti & Rees 1996; Hirotani et al. 1999; Sikora & Madejski 2000; Kino, Takahara & Kusunose 2002 (hereafter KTK02); Asano & Takahara 2003). In the case of e^\pm plasma, the shock first converts bulk population of particles into thermal ones and accelerates some of them from this thermal pool where $\Gamma_{43}\rho_{ec}c^2 \sim P = n_{ek}T_e \sim \gamma_{\min}\rho_{ec}c^2$, then it leads to $\gamma_{\min} \simeq \Gamma_{43}$. On the other hand, in the case of ep plasma, there is wide variety of possibilities about γ_{\min} . One extreme case is that protons and electrons are separately thermalized where $\Gamma_{43}\rho_{pc}c^2 \sim P \simeq n_{pk}T_p$, $\Gamma_{43}\rho_{ec}c^2 \sim P_e = n_{ek}T_e \sim \gamma_{\min}\rho_{ec}c^2$, and $T_e = (m_e/m_p)T_p$, which also leads to $\gamma_{\min} \simeq \Gamma_{43}$. The other extreme case is that thermal energy of protons is quickly transferred to electrons and they attain one temperature state $\Gamma_{43}\rho_{pc}c^2 \sim P = 2n_{pk}T_p \sim \gamma_{\min}\rho_{ec}c^2$, which leads to $\gamma_{\min} \simeq \frac{m_p}{m_e}\Gamma_{43}$. To make the argument clear, here we only treat these three extreme cases as follows;

- (i) The plasma consists of pure e^\pm (Case I).
- (ii) The plasma consists of pure ep with no energy transfer from protons to electrons, which leads to two temperature state $T_i \neq T_e$ (Case II).
- (iii) The plasma consists of pure ep with quick energy transfer from protons to electrons and one temperature state $T_i = T_e$ is realized (Case III).

We omit intermediate cases. Summing up, we have γ_{\min} as

$$\gamma_{\min} \simeq \begin{cases} \Gamma_{43} & \text{(Case I, Case II)} \\ \frac{m_p}{m_e}\Gamma_{43} & \text{(Case III).} \end{cases} \quad (13)$$

Correspondingly, the rest mass density of shock-accelerated electrons is given by

$$\begin{aligned} \rho_{3,acc} &= m_e n_{3,acc} \\ &= m_e \int_{\gamma_{\min}}^{\gamma_{\max}} K \gamma^{-s} d\gamma \\ &\simeq \begin{cases} K m_e \Gamma_{43}^{-1} & \text{(Case I, Case II)} \\ K m_e \frac{m_p}{m_e} \Gamma_{43}^{-1} & \text{(Case III)} \end{cases} \end{aligned} \quad (14)$$

where K is the normalization factor of the relativistic electron number density and $s = 2$ is adopted. Using the injection rate of relativistic electrons q_e and adiabatic loss time-scale t_{esc} , it is written as $K = t_{\text{esc}}q_e$ (e.g., Mastichiadis & Kirk 1997; KTK02). The energy density of shock-accelerated electrons is given by

$$\begin{aligned} U_{3,acc} &= (\langle \gamma \rangle - 1) n_{3,acc} m_e c^2 \\ &\simeq m_e c^2 \int_{\gamma_{\min}}^{\gamma_{\max}} K \gamma^{-s+1} d\gamma \\ &\simeq \begin{cases} K m_e c^2 \ln \frac{\gamma_{\max}}{\Gamma_{43}} & \text{(Case I, Case II)} \\ K m_e c^2 \ln \frac{m_e}{m_p} \frac{\gamma_{\max}}{\Gamma_{43}} & \text{(Case III)} \end{cases} \end{aligned} \quad (15)$$

where $s = 2$ is adopted.

From the observed non-thermal spectra, we can obtain the number and energy densities of accelerated electrons. From the hydrodynamical shock condition, we independently obtain the number and energy densities of total particles. Hence we can express ϵ and ζ as a function of a single parameter Γ_4 . Then the obvious condition $1 \geq \zeta$ is

rewritten as

$$1 \geq \frac{20}{9} \frac{\mathcal{M}_1^2}{5\mathcal{M}_1^2 - 1} \frac{(\Gamma_{43} - 1)}{\beta_{FS}^2} \frac{n_{3,acc}}{n_{ICM}} \frac{m_e}{m_p} \simeq \begin{cases} \frac{4}{3(5\mathcal{M}_1^2 - 1)} \frac{K m_e c^2}{P_1} \left(1 - \frac{1}{\Gamma_{43}}\right) & \text{(Case I, Case II)} \\ \frac{4}{3(5\mathcal{M}_1^2 - 1)} \frac{K m_e c^2}{P_1} \left(1 - \frac{1}{\Gamma_{43}}\right) \frac{m_e}{m_p} & \text{(Case III)} \end{cases} \quad (16)$$

and the condition $1 \geq \epsilon$ can be written as

$$1 \geq \frac{20}{9} \frac{\mathcal{M}_1^2}{5\mathcal{M}_1^2 - 1} \frac{(\langle \gamma \rangle - 1)}{\beta_{FS}^2} \frac{n_{3,acc}}{n_{ICM}} \frac{m_e}{m_p} \simeq \begin{cases} \frac{4}{3(5\mathcal{M}_1^2 - 1)} \frac{K m_e c^2}{P_1} \ln \left(\frac{\gamma_{\max}}{\Gamma_{43}} \right) & \text{(Case I, Case II)} \\ \frac{4}{3(5\mathcal{M}_1^2 - 1)} \frac{K m_e c^2}{P_1} \ln \left(\frac{m_e}{m_p} \frac{\gamma_{\max}}{\Gamma_{43}} \right) & \text{(Case III)} \end{cases} \quad (17)$$

From this, we stress an important point that ζ and ϵ have very weak dependence on Γ_4 through Γ_{43} . This is understood as follows.

Given the ICM physical quantities and hot spot advance speed, P_3 is fixed from Eqs. (1) and (3). When the jet speed is relativistic, we obtain the relation $P_3 \propto \Gamma_{43}\rho_3 \sim \Gamma_4\rho_3$. Therefore, we have the relation $\rho_3 \propto \Gamma_4^{-1}$. On the other hand, $\rho_{3,acc}$ is given by $\rho_{3,acc} \propto \gamma_{\min}^{-s+1} \propto \Gamma_4^{-1}$ for $s = 2$. Thus ζ has only a weak dependence on Γ_4 . Next we consider ϵ . The average Lorentz factor of relativistic electrons is $\langle \gamma \rangle \propto \gamma_{\min} \ln(\gamma_{\max}/\gamma_{\min})$. Then combining these relations, we can see $\epsilon \propto \langle \gamma \rangle \propto \zeta/\Gamma_{43} \propto \ln(\gamma_{\max}/\Gamma_4)$, therefore ϵ has also a weak dependence on Γ_4 .

So far, we have two constraints on the energetics and plasma composition of jets, i.e., $\epsilon \leq 1$ and $\zeta \leq 1$. Another constraint is $n_{3,tot} \geq n_{3,acc}$ which is written as

$$1 \geq \frac{n_{3,acc}}{n_{3,tot}} \simeq \begin{cases} \frac{\zeta}{\frac{m_p}{m_e}\zeta} & \text{(Case I, Case III)} \\ \frac{m_p}{m_e} & \text{(Case II).} \end{cases} \quad (18)$$

By these three constraints, we investigate the physical condition of FR II jets in the next section.

3 APPLICATION

We explore the energetics related with non-thermal electrons. As specific FR II sources, we deal with Cygnus A and 3C 123. The nearby radio galaxy Cygnus A (z=0.0562) is well known as the very powerful radio galaxy. Recent observation with the *Chandra X-ray Observatory* resolves the X-ray emission from the two brighter hot spots (A and D) by Wilson et al (2000) with sufficiently high angular resolution $\sim 0.5''$. We adopt the observational data of spot A compiled by Wilson et al (2000). 3C 123 ($z = 0.2177$) is famous for its high luminosity and peculiar radio structure. The lobes take the form of diffuse twisted plumes unlike those in any other well-known sources (e.g., Riley & Pooley 1978; Hardcastle et al. 1997). We adopt the observational data including *Chandra*'s one compiled by Hardcastle et al (2001). After this preparation, in §3.2, we apply the method in the previous section to the representative FR II jet Cygnus A and constrain the energetics and plasma contents. Since the advance

speed of hot spot in 3C 123 is not constrained so far, we do not treat the case of 3C 123 in this work. We use $H_0 = 50 \text{ km s}^{-1} \text{ Mpc}^{-1}$ and $q_0 = 0$ throughout this paper.

3.1 Non-thermal Emission from Hot Spots

Using the observed spectrum from hot spots, we can determine the physical quantities related with non-thermal electrons. The purpose of this section is to explore the energetics in the hot spots based on the multi-frequency spectra. Here we identify the hot spot as the region 3 and identify the ICM as the region 1, as shown in Figure 1.

The first point to be discussed is the X-ray emission mechanism from hot spots. A thermal model tends to require much higher densities than the upper limit obtained by the absence of Faraday depolarization in hot spots. Therefore, non-thermal emission is most plausible for X-ray emission from these hot spots. Next, we must check the relative importance of the seed photons for inverse Compton scattering. The energy density of locally produced synchrotron photons in the hot spots is $U_{\text{syn}} = \frac{3L_{\text{syn}}}{4\pi R^2 c} = 8 \times 10^{-11} \left(\frac{L_{\text{syn}}}{10^{44} \text{ erg s}^{-1}} \right) \left(\frac{R}{1 \text{ kpc}} \right)^{-2} \text{ erg cm}^{-3}$ where R is the size of the hot spot and we set $L_{\text{syn}} = L_{\text{syn,o}}$ because the advance speed of the hot spots is inferred to be non-relativistic. The cosmic microwave background (CMB) energy density is given by $U_{\text{CMB}} = aT_{\text{CMB}}^4(1+z)^4 = 4.2 \times 10^{-13}(1+z)^4 \text{ erg cm}^{-3}$ where a is the radiation constant. Compared to U_{syn} , U_{CMB} is safely negligible. Alternatively, the importance of other seed photon sources for IC scattering has been suggested for X-rays from radio lobes (not a hot spot) (e.g., Brunetti et al. 2001). It is likely that there is a strongly beamed emission from the blazar jet in the nucleus, which comes along the jet axis and is injected into the hot spots. Hence it must be checked if this process is effective or not. Although we cannot directly observe the beamed emission from the inner sub-parsec jet (i.e., blazar) of FR II radio galaxies, unified schemes for AGNs (e.g., Urry & Padovani, 1995) suggest that the inner jets should have the same properties as quasar-hosted blazars (QHB). The observed bolometric synchrotron luminosity of QHB $L_{\text{syn,o,core}}$ is evaluated by Kubo et al. (1998) and typically $L_{\text{syn,o,core}} \sim 10^{47} \text{ erg s}^{-1}$. Thus, the injected synchrotron photon energy density is $U_{\text{syn,core}} = \frac{L_{\text{syn,o,core}}}{4\pi D_{\text{HS}}^2 c} = 1 \times 10^{-12} \left(\frac{L_{\text{syn,o,core}}}{10^{47} \text{ erg s}^{-1}} \right) \left(\frac{D_{\text{HS}}}{100 \text{ kpc}} \right)^{-2} \text{ erg cm}^{-3}$ where D_{HS} is the distance of the hot spot from the core. Only when an extremely luminous blazar component is hidden and/or D_{HS} is fairly small, $U_{\text{syn,core}}$ component is dominant as seed photons. In this paper, we treat the case of $U_{\text{syn}} > U_{\text{syn,core}}$ which seems to be plausible for hot spot sources observed by Chandra. (The case of $U_{\text{syn}} < U_{\text{syn,core}}$ is discussed by Brunetti et al. 2001.) Therefore it seems reasonable to suppose that seed photons of inverse Compton X-rays are synchrotron-dominated and we adopt the synchrotron-self Compton (SSC) model in this paper as in most of the previous works.

Before we get on the issue of SSC model, we describe our naming on non-thermal electron distributions used in this paper. When the radiative cooling time is shorter than the adiabatic expansion loss time of electrons t_{esc} , the electron spectrum steepens by 1 in the power law index because

the cooling time is inversely proportional to the energy. According to the value of γ_{br} which describes the break of the electron Lorentz factor by radiative cooling, we can classify relativistic electron spectra into three regimes. Schematic pictures of the electron spectra are shown in Figure 2. If $\gamma_{\text{br}} > \gamma_{\text{max}}$, we call it *weak cooling regime* and if $\gamma_{\text{br}} < \gamma_{\text{min}}$, we call it *moderate cooling regime*, and if $\gamma_{\text{br}} < \gamma_{\text{min}}$, we call it *strong cooling regime*, in this paper. In comparison with the conventional terminology of these cooling regimes which Sari, Piran & Narayan (1998) originally named in the study of GRB afterglows, strong cooling corresponds to fast cooling, while moderate cooling corresponds to slow cooling. In their study, there is no counterpart for weak cooling. But we need to consider this situation for hot spots. Hence, in this work, we renamed these cooling regimes.

3.1.1 Analytic Estimations

It is useful to estimate the model parameter analytically since it gives us a good insight into the physics behind the relationship between the model parameters and typical observables. Hence we describe some analytic estimates of the model parameters following the method of KTK02 and Kino (2002) before presenting numerical results.

In the case of hot spots, we can directly observe the emission region size R , and we can set the Doppler factor $\delta = 1$. The other three parameters, B , γ_{max} , and q_e remain to be determined. The three typical observables in the observer frame are: $\nu_{\text{syn,o,max}}$ the maximum synchrotron frequency, $L_{\text{syn,o}}$ total synchrotron luminosity, and $L_{\text{ssc,o}}$ total SSC luminosity. For example observables of hot spots of Cygnus A are $F_{\text{syn}} \sim 1 \times 10^{-11} \text{ erg s}^{-1} \text{ cm}^{-2}$, and $F_{\text{ssc}} \sim 5 \times 10^{-13} \text{ erg s}^{-1} \text{ cm}^{-2}$ (obtained from the direct integration of the multi-band spectrum). As for the $\nu_{\text{syn,o,max}}$, we cannot define a strict value from the observed data since IR and optical data only give upper limits. Here we tentatively set $\nu_{\text{syn,o,max}} \sim 10^{11} \text{ Hz}$, although some suggest higher “cut-off” frequencies close to $\sim 10^{13} \text{ Hz}$ (e.g., Carilli et al. 1999). Since Eqs. (14) and (15) have weak dependence on γ_{max} , no significant effect is expected on the electron acceleration efficiency. Observed total flux, typical frequencies, and luminosity distance are scaled as

$$f_{\text{syn}} = \frac{F_{\text{syn,o}}}{10^{-11} \text{ erg s}^{-1} \text{ cm}^{-2}}, \quad f_{\text{ssc}} = \frac{F_{\text{ssc,o}}}{10^{-12} \text{ erg s}^{-1} \text{ cm}^{-2}}, \quad (19)$$

and

$$\nu_{\text{syn}} = \frac{\nu_{\text{syn,o,max}}}{10^{11} \text{ Hz}}, \quad r = \frac{R}{1 \text{ kpc}}, \quad d = \frac{D_{\text{L}}}{100 \text{ Mpc}}. \quad (20)$$

Using Eqs. (7), (10), and (11) in KTK02 which connect the observables and model parameters, we obtain

$$B = 5.0 \times 10^{-5} f_{\text{syn}} f_{\text{ssc}}^{-1/2} r^{-1} \text{ G}, \quad (21)$$

and

$$\gamma_{\text{max}} = 1.3 \times 10^5 f_{\text{syn}}^{-1/2} f_{\text{ssc}}^{1/4} \nu_{\text{syn}}^{1/2} r^{1/2}. \quad (22)$$

Next, we must discuss the break Lorentz factor γ_{br} which appears in the electron spectrum. The one-zone SSC model with electron escape on a finite time scale predicts that the break Lorentz factor γ_{br} appears at an energy where $t_{\text{esc}} = t_{\text{cool}}$. From this, we obtain $\frac{R}{C_1 c} = \frac{3m_e c}{4(U_B + U_{\text{syn}})\sigma_T \gamma_{\text{br}}}$ where C_1

expresses the adiabatic expansion loss. Then, cooling break in the electron spectrum can be written as follows;

$$\gamma_{\text{br}} = 1.0 \times 10^6 f_{\text{syn}}^{-2} f_{\text{ssc}} \left(1 + \frac{f_{\text{ssc}}}{f_{\text{syn}}} \right)^{-1} r c_1, \quad (23)$$

where $c_1 = 3C_1$ and this is reasonable when the escape speed is comparable to the relativistic sound speed. In the moderate cooling regime, we have

$$K = \frac{L_{\text{syn,o}}}{4\pi R^3/3} \times \left[\frac{4}{3} \sigma_T c U_B \int_{\gamma_{\text{min}}}^{\gamma_{\text{br}}} \gamma^{-s+2} d\gamma + \frac{m_e c^2}{t_{\text{esc}}} \left(1 + \frac{f_{\text{ssc}}}{f_{\text{syn}}} \right)^{-1} \int_{\gamma_{\text{br}}}^{\gamma_{\text{max}}} \gamma^{-s+1} d\gamma \right]^{-1} \text{cm}^{-3}. \quad (24)$$

where $K = q_e t_{\text{esc}}$. For the weak cooling regime, no break feature appears in the spectrum. In this case, q_e is written

$$K = \frac{L_{\text{syn,o}}}{4\pi R^3/3} \left[\frac{4}{3} \sigma_T c U_B \int_{\gamma_{\text{min}}}^{\gamma_{\text{max}}} \gamma^{-s+2} d\gamma \right]^{-1} \text{cm}^{-3}. \quad (25)$$

Clearly, if $\gamma_{\text{br}} = \gamma_{\text{max}}$, Eqs. (24) and (25) give the same value of q_e .

In order to check which regime is realized for each hot spot, we analytically estimate γ_{br} and γ_{max} and compare them for $c_1 = 1$. Adopted observables are shown in Table 1 and the resultant γ_{br} and γ_{max} are shown in Table 2. As it turns out, weak cooling is plausible for these hot spots within this order of estimation.

By analytic estimation of Eqs. (23) and (22), we can see that weak cooling or marginally moderate cooling is plausible for typical hot spots. The case of $\gamma_{\text{br}} \sim 10^2 - 10^3$ is not appropriate, since the theoretically predicted spectrum for this case underlies below the observed radio spectrum.

3.1.2 Numerical Fitting Results for Cygnus A and 3C123

Numerical calculations are the best way to obtain the exact electron energy spectrum and here we show the numerical fitting results of observed multi-frequency spectra in hot spots. The detailed treatment of synchrotron and inverse Compton scattering processes is shown in KTK02. Note that, in our model, the injected power law electron spectrum does not have a sharp cut-off but have an exponential cut-off such as $\gamma^{-s} \exp(-\gamma/\gamma_{\text{max}})$ (e.g., Mastichiadis & Kirk 1997; KTK02).

The thick solid curve in Figure 3 shows the best fit spectrum for the hot spot A in Cygnus A obtained by the one-zone SSC model for $\gamma_{\text{min}} = 1$ and $c_1 = 1$. Corresponding physical parameters are shown in Table 3. Comparing these parameter values with those obtained by the analytic estimation (Table 2), we find that analytic estimation in the previous subsection is a good approximation. The important result is that $U_{3,\text{acc}}/U_B = 7$ in the hot spot A for $\gamma_{\text{min}} = 1$ (this roughly corresponds to Case I and Case II since Γ_{43} is an order of unity). This means that the kinetic power is dominated in the hot spots similar to the case of TeV blazars (KTK02). In order to check the Case III, we examine the case of $\gamma_{\text{min}} \sim 2000$, and this is drawn by a dotted line. In this case, we have $U_{3,\text{acc}}/U_B = 0.8$. As we can see in Figure

3, predicted flux is below the observed one below $\sim 10^{10}$ Hz and for Chandra X-ray data. Hence, we rule out the Case III.

The thick solid curve in Figure 4 shows the best fit spectrum for the eastern hot spot in 3C 123 obtained by the one-zone SSC model for $\gamma_{\text{min}} = 1$ and $c_1 = 1$. Although the radio spectrum is rather poorly fitted, this does not much affect our conclusions as discussed later in this subsection. As is for Cygnus A, by comparing Table 4 with Table 2, we find that analytic estimation in the previous subsection is a good approximation. The important result is that $U_{3,\text{acc}}/U_B = 18$ for 3C 123. This means that the kinetic power is dominated in the hot spots similar to the case of TeV blazars (KTK02) and Cygnus A hot spot. Similar to the case of Cygnus A, we examine the case of $\gamma_{\text{min}} \sim 2000$, we have $U_{3,\text{acc}}/U_B = 3$ and also we rule out the Case III for 3C 123.

To sum up, we find that the energy density of relativistic electrons is about one order of magnitude larger than that of magnetic field which means that conventional *minimum energy hypothesis* is not strictly true in these hot spots. We can also find that relatively low $\gamma_{\text{min}} \sim$ a few is preferred based on the SSC model fitting. In this case, energy density of non-thermal electrons is about one order of magnitude larger than that of magnetic fields. Hence, we conclude that the assumption of neglecting the magnetic effects in the shock jump condition in §2 is a correct one. Additional new finding in this spectral calculation is that the twice-scattered Compton component is predicted for these sources in the GeV energy band. If this bump can be detected in future observations, it must give strong constraints on physical quantities in these hot spots. However the predicted flux does not reach the detection threshold of *GLAST*.

Compared with previous works, for Cygnus A, the resultant physical quantities and energy densities in this paper are almost the same as the result of Wilson, Young, & Shopbell 2000). According to their adopted value for the hot spot A, their result leads to $U_{3,\text{acc}}/U_B \sim 4$. A difference between the present work and the work of Wilson, Young, & Shopbell 2000 is that they adopted $\gamma_{\text{br}} \simeq 4 \times 10^3$, while we show that weak cooling regime is consistent with observations (see below as for a solution in moderate cooling regime) by solving the electron kinetic equation both analytically and numerically. We find that low radiative efficiency by comparing relativistic electron energy and radiation field energy. For 3C 123, Hardcastle, Birkinshaw, & Worrall (2001) regard that magnetic fields strength in the hot spot is consistent with being equipartition by assuming $\gamma_{\text{min}} \simeq 1000$. This roughly corresponds to the case of *ep* plasma composition with one temperature for which $\gamma_{\text{min}} \sim m_p/m_e$. This assumption seems to contradict with their another assumption that no relativistic protons are contained in the spot.

Let us examine whether the above results depend on the assumption of $c_1 = 1$ since predicted radio spectra show only a global matching with the observed one. Some of the previous work reported the existence of the spectral break in the radio band for Cygnus A (Meisenheimer et al. 1997) and 3C123 (Looney & Hardcastle 2000). To reproduce a cooling break (to enter the moderate cooling regime), the smaller value of c_1 is required. Hence we examine the case of smaller c_1 . We select the case of $c_1 = 1/6$ which corresponds to the case of escape velocity 0.055c for the spot A (Carilli et al. 1999). Although most of the effects of smaller c_1 are

absorbed by a decrease of q_e , the decrease of high energy electrons leads to a decrease of high energy portion of the synchrotron spectrum. To compensate for this, somewhat higher γ_{\max} and B will be required compared to the case of $c_1 = 1$. The numerical results are tabulated in Tables 3 and 4 and predicted spectra are shown in Figs. 3 and 4 by thin solid curves.

For Cygnus A, the differences in the resultant parameters between the cases of $c_1 = 1$ and $c_1 = 1/6$ are very small as is seen in Table 3. The spectral fitting reproduces equally well the observations for $c_1 = 1/6$ and $\gamma_{\min} = 1$ as shown in Fig. 3 by the thin solid line. The case with large γ_{\min} under-predicts low frequency radio and SSC X-ray fluxes as is seen in Fig. 3 by the thin dotted line and is ruled out. For 3C123, the differences are within a factor of 2 as is seen in Table 4; the magnetic field strength is 45% larger and $U_{3,\text{acc}}/U_B$ is smaller by a factor of 2 for $c_1 = 1/6$ than for $c_1 = 1$. However, the spectral fitting is not significantly improved even for $c_1 = 1/6$ and $\gamma_{\min} = 1$ as shown in Fig. 4 by the thin solid line. Although the prediction better reproduces high energy radio spectrum, it is well above low frequency radio data. For $c_1 = 1/6$ and $\gamma_{\min} = 2000$ whole synchrotron spectra are better fitted but the SSC flux in the X-ray band is below the observation. In this sense, $c_1 = 1/6$ and intermediate γ_{\min} may best reproduce the observed data, although we do not further pursue this point in this paper. If this is the case, $U_{3,\text{acc}}/U_B$ becomes smaller, but still greater than 1.

3.2 Physical Condition of Cygnus A

3.2.1 Known Quantities

Here we investigate the plasma content and electron acceleration efficiency in Cygnus A hot spot which is well known as the best candidate for studying the nature of FR II radio source. Regarding the unshocked ICM, the continuous study of the X-ray observations reveals its temperature and number density (Arnaud et al. 1984; Ueno et al. 1994; Smith et al. 2002). Here, we adopted the the number density and temperature of Cygnus A cluster as $\rho_1 = m_p n_{\text{ICM}} \simeq 10^{-2} m_p \text{ g cm}^{-3}$ and $T_1 \simeq 4 \times 10^7 \text{ K}$ shown in Arnaud et al. (1984). Then we have the ICM pressure by $P_1 = 2n_{\text{ICM}} k T_{\text{ICM}}$. The velocity of the fluid in the upstream is $v_1 = 0$ by definition. Hence we can obtain three downstream quantities of the forward shock based on the ICM observations. About the unshocked jet, we assume $P_4 = 0$. The advance speed of the hot spot β_{HS} has been estimated by synchrotron spectral aging methods (Carilli & Barthel 1996; for review), $\beta_2 = \beta_3 = \beta_{\text{HS}}$. We use the value of v_3 taking into account an uncertainty of about one order of magnitude. In the present work, we examine the case of $0.01c < v_3 < 0.1c$. In other words, we take account the uncertainty in v_3 instead of B as is the synchrotron aging methods (e.g., Carilli et al. 1991). The velocity of the unshocked jet $\Gamma_4 \beta_4$ is not directly measured. The upper limit of the jet velocity is inferred from the initially ejected jet speed corresponding to the sub-parsec scale jet (i.e., blazars) velocity and the upper limit of Γ_4 is taken to be about 30 (e.g., KTK02). With regard to the lower limit of the jet velocity, we set the minimum value as $\Gamma_4 > 3$ for simplicity. Note that recent statistical studies of measurements of

jet-to-counter jet flux ratio in FR II sources imply that the minimum Γ_4 is close to unity (e.g., Wardle & Aaron 1997; Hardcastle et al. 1999). Thus we can fix 5 quantities such as ρ_1 , P_1 , v_1 , v_3 and P_4 . Then, we solve 6 physical quantities such as ρ_2 , $P_2 = P_3$, ρ_3 , ρ_4 , v_{FS} , and v_{RS} as a function of Γ_4 by following the procedure shown in the previous section. As for the non-thermal electrons, based on the result in the previous subsection, we examine the case of $s = 2.1$, $\gamma_{\max} = 1 \times 10^4$, and $K = 1 \times 10^{-3} \text{ cm}^{-3}$ based on Table 3. As for the relativistic electron number density $n_{3,\text{acc}}$ and normalization K , here we use the value of $\gamma_{\min} = 1$ in Table 3, then we have $n_{3,\text{acc}} \sim K \gamma_{\min}^{-1}$. Our resultant value of K and the one obtained by Wilson et al. (2000) is consistent with each other.

3.2.2 Mass Density of the Jet

Figure 5 shows rest mass density ratio of the unshocked jet to the unshocked ICM. It should be stressed that ρ_4 is not a free parameter but a solvable quantity as is shown in §2. For $\Gamma_4 \gg 1$, one can see $\rho_4 \propto \beta_{\text{HS}}^2 \Gamma_{43}^{-2}$. In Fig. 5 the shaded region corresponds to $0.01 < \beta_{\text{HS}} < 0.1$. At $\Gamma_4 \sim 3$, $\beta_{\text{HS}} = 0.1$ (which corresponds to relatively large Mach number $\mathcal{M}_1 \simeq 50$) leads to $f \sim 10^{-3}$ while $\beta_{\text{HS}} = 0.01$ (corresponds to $\mathcal{M}_1 \simeq 5$) shows $f \sim 10^{-5}$. Given Γ_4 , allowable range of the rest mass density ρ_4 spans about two order of magnitude because β_{HS} is uncertain by one order of magnitude. For fixed β_{HS} , as Γ_4 increases, the density decreases according to $\rho_4 \propto \Gamma_{43}^{-2} \propto \Gamma_4^{-2}$. From this, we can directly see that the jet is very light for all range of Γ_4 .

Let us compare these results with the previous works. Many authors have done the numerical simulation of extra-galactic jets (e.g., Norman, Smarr, Winkler & Smith 1982; Clarke, Norman, & Burns 1986; Marti et al. 1997) and it has been found that light jets are required for producing cocoon structures (e.g., Norman, Smarr, Winkler & Smith 1982; Komissarov & Falle 1998). Although most of previous works have studied mainly the range of $10^{-2} < f$ (e.g., Cioffi & Blondin 1992), a study of *very light jet* has been recently reported by Krause (2003). He examined the range of $10^{-5} < f < 10^{-2}$ which has not been studied so far but matches with our result. Based on the morphology of Cygnus A obtained by Chandra (Smith et al. 2002), they claimed that $f < 10^{-3}$ which agrees well with our result although their work and ours are definitely different approaches for estimating the mass density of the jet. We should add to note that, the lightness of the jet is consistent with the relativistic speed of the jet and the non-relativistic advance speed of the hot spot.

3.2.3 Total Kinetic Power of the Jet

Figure 6 shows the jet power compared with the Eddington power. The total jet kinetic power is defined as

$$L_{\text{kin}} = \pi R_{\text{HS}}^2 \Gamma_4^2 \beta_4 \rho_4 c^2 \quad (26)$$

Similar to Fig. 5, the important point is that total kinetic power L_{kin} in Cygnus A is not a free parameter but consistently obtained by solving ρ_4 for given Γ_4 . As $L_{\text{kin}} \propto \beta_{\text{HS}}^2$, the allowed range of the total jet kinetic power spans about two order of magnitude. The reason for weak dependence

on Γ_4 is already shown in §2, so we do not repeat it here. Compared with the Eddington power, when a hot spot has relatively high advance speed of $0.1c$, the jet power exceeds the Eddington power even for a relatively heavy black hole mass $10^9 M_\odot$. This may suggest that the hot spot advance speed is slower than $0.1c$.

Compared with the other FR II sources, kinetic power of Cygnus A with $\beta_{HS} = 0.1$ is by a factor of a few larger than that of brightest FR II sources reported in Figure 1 of Rawlings & Saunders (1991). So Cygnus A is one of the most brightest FR II sources in low-redshifts $z < 0.5$ not only in the radio band (Carrili & Barthel 1996) but also in the kinetic power. Related to this, flat spectrum radio quasars (FSRQs) are believed to be the inner core part jet (typically sub-pc scales) of the FR II sources (Urry & Padovani 1995). Then, the total kinetic power of this core region estimated by the SSC analysis as $L_{\text{kin,core}} \sim L_{\text{syn,core,o}}/\Gamma^2 \sim 10^{45} \text{ erg s}^{-1}$. Here we used the data of brightest FSRQs $L_{\text{syn,core,o}} \sim 10^{47} \text{ erg s}^{-1}$ in Kubo et al. (1998) and assume $\Gamma \sim 10$. Using this,

$$10^{-3} < \frac{L_{\text{kin,core}}}{L_{\text{kin}}} < 10^{-1} \quad (27)$$

Within the framework of internal-external shock scenario (e.g., Piran 1999), the value $\frac{L_{\text{kin,core}}}{L_{\text{kin}}}$ almost equals to the ratio of the dissipation rate by the internal shock to that of the external shock, only a small fraction of total kinetic power from the central engine is dissipated in sub-pc scales and most of the bulk kinetic power remains up to 100kpc scales and then is dissipated by strong deceleration by the ICM pressure. If the adopted core luminosity estimate is acceptable, then our estimate shows suitable agreement with the internal-external shock scenario similar to the case of GRBs.

3.2.4 Electron Acceleration Efficiency

Figure 7 shows the energy density ratio of accelerated electrons to total particles in Cygnus A hot spot (spot A). In the same way as mass density and kinetic power of the jet, allowable range of ϵ spreads over two order of magnitude as about $10^{-2} < \epsilon < 1$ because of the uncertainty of hot spot advance speed. We see that the case of $\beta_{HS} < 0.01$ does not satisfy the constraint Eq. (17) and is ruled out. It should be noted that if we definitely determine β_{HS} of Cygnus A as close as 0.01 in the future, then we must reconsider the shock structure taking the back-reaction of accelerated electrons into account (e.g., Drury & Voelk 1981; Malkov 1997). If $\beta_{HS} \sim 0.1$ is confirmed, then we can employ the simplest test particle theory for the Cygnus A spot. It is also worth noting that in the case of the rapidly advancing hot spot $\beta_3 \sim 0.1$ the result shows the existence of missing thermal power which is about two orders of magnitude larger than that of accelerated electron kinetic power.

It is well known that there is a major gap which separates numerical simulations from direct comparison with observed image. The gap is that we have little knowledge about the relativistic electron production rate (e.g., Krolik 1999). We again stress that one of most important achievements of our work is that we show the simple method to remove this difficulty and estimate electron acceleration efficiency.

3.2.5 Plasma Composition

Figure 8 shows the number density ratio of accelerated electrons to total particles in the hot spot. In the case of e^\pm plasma, we estimate $n_{3,\text{acc}}/n_3 = \zeta$. In the case of two-temperature ep plasma, we estimate $n_{3,\text{acc}}/n_3 = 1837\zeta$. In the spot in Cygnus A, we find that if the plasma is composed of a two temperature ep plasma (Case II), the number density of accelerated electrons exceeds that of thermal particles. Fermi acceleration predicts that some fraction of thermal particles is converted into relativistic particles. Hence we can exclude the case of $n_{3,\text{acc}}/n_3 > 1$ by definition. Hence, we can derive the important result that a two temperature ep plasma composition is ruled out. In Figure 9, we summarize this plasma composition diagnosis. Combined with the result of rejection of one-temperature ep plasma (Case III) by the spectrum fitting result for Cygnus A, we draw the conclusion that only e^\pm plasma is acceptable for the Cygnus A hot spot.

4 CONCLUSIONS

To sum up, we investigate the energetics and plasma composition in FR II sources using a new simple method of combining shock dynamics and radiation spectrum. For simplicity, we examine three extreme cases of pure electron-positron pair plasma (Case I), pure electron-proton plasma with separate thermalization (Case II), and pure electron-proton plasma in thermal-equilibrium (Case III).

Based on the SSC model with escape velocity as $c_1 = 3v_{\text{esc}}/c = 1$ (roughly corresponds to weak cooling) and $c_1 = 1/6$ (roughly corresponds to moderate cooling), we estimate the number and energy densities of non-thermal electrons using the multi-frequency radiation spectrum of hot spots. The results of SSC analysis for the hot spots of Cygnus A and 3C 123 (see Figures 3 and 4; Tables 2 and 3) are as follows:

- The energy density of relativistic electrons is about 10 times larger than that of magnetic fields.
- For Cygnus A, we find that both of the $c_1 = 1$ and $c_1 = 1/6$ with $\gamma_{\min} = 1$ explain the observation. In both cases, the radiative efficiencies are low (typically $\sim 1\%$) and resultant parameters are very similar. Case III is not acceptable because predicted photon spectra do not give a good fit to the observed one.
- For 3C123, $c_1 = 1$ with $\gamma_{\min} = 1$ gives a global fit to the observations although detailed radio spectrum is rather poorly fit. The $c_1 = 1/6$ of $\gamma_{\min} = 2000$ gives a better fit on the radio spectrum but underpredict the X-ray flux. The difference between Cygnus A and 3C123 is an interesting open issue.

Independently, with the 1D shock jump conditions taking account of the finite pressure of hot ICM, we estimate the rest mass and energy densities of the sum of thermal and non-thermal particles in hot spots. We utilize the condition that the obtained rest mass, internal energy, and number densities of non-thermal electrons should be lower than those of the total particles determined by shock dynamics. The results of the energetics and plasma composition by using our new method for Cygnus A in the range of $3 < \Gamma_4 < 30$ are as follows:

- We estimate the ratio of jet rest mass density to that of ICM by solving the shock jump conditions. We find that the jet is very light $10^{-7} < f < 10^{-3}$.
- The total jet kinetic power is examined. We found that it has the kinetic power of about $10^{46} < L_{\text{kin}} < 10^{48} \text{ erg s}^{-1}$.
- We examine the electron acceleration efficiency in the hot spot. We found that the efficiency is about $0.01 < \epsilon < 1$.
- Plasma composition is investigated. We find that both pure two temperature *ep* plasma (Case II) and pure one temperature *ep* plasma (Case III) can be ruled out. Hence we conclude that the plasma composition is most likely to be e^\pm dominated.

ACKNOWLEDGMENTS

We thank the anonymous referee for his/her helpful comments. We thank M. Kusunose for providing us with the numerical code. M.K. grateful S. Yamada and A. Mizuta for helpful discussions on shock dynamics and N. Isobe for useful comments on observational issues. F.T. acknowledges the Grant-in-Aid for Scientific Research of the Japanese Ministry of Education, Culture, Sports, Science and Technology, No. 13440061, 14079025, and 14340066.

REFERENCES

Arnaud K. A., Fabian A. C., Eales S. A., Jones C., Forman W., 1984, MNRAS, 211, 981

Asano K.,& Takahara F., 2003, PASJ, 55, 433

Brunetti, G., Cappi, M., Setti, G., Feretti, L., & Harris, D. E. 2001, A&A, 372, 755

Begelman, M. C. & Cioffi, D. F. 1989, ApJL, 345, L21

Blandford, R. D. & McKee, C. F. 1976, Physics of Fluids, 19, 1130

Carilli, C. L., Perley, R. A., Dreher, J. W., & Leahy, J. P. 1991, ApJ, 383, 554

Carilli, C. L. & Barthel, P. D. 1996, A&ARv, 7, 1

Carilli C. L., Perley R., Harris D. E., Barthel P. D., 1998, PhPl, 5, 1981

Carilli C. L., Kurk J. D., van der Werf P. P., Perley R. A., Miley G. K., 1999, AJ, 118, 2581

Cioffi D. F., Blondin J. M., 1992, ApJ, 392, 458

Clarke D. A., Norman M. L., Burns J. O., 1986, ApJL, 311, L63

Drury, L. O. & Voelk, J. H. 1981, ApJ, 248, 344

Falle S. A. E. G., 1991, MNRAS, 250, 581

Georganopoulos M., Kazanas D., 2003, ApJ, 589, L5

Harris D. E., Nulsen P. E. J., Ponman T. J., et al., 2000, ApJ, 530, L81

Hardcastle M. J., Alexander P., Pooley G. G., Riley J. M., 1997, MNRAS, 288, 859

Hardcastle M. J., Alexander P., Pooley G. G., Riley J. M., 1999, MNRAS, 304, 135

Hardcastle, M. J., Birkinshaw, M., & Worrall, D. M. 2001, MNRAS, 323, L22

Hardcastle M. J., Birkinshaw M., Cameron R. A., Harris D. E., Looney L. W., Worrall D. M., 2002, ApJ, 581, 948

Hirotani K., Iguchi S., Kimura M., Wajima K., 1999, PASJ, 51, 263

Kaiser C. R., Alexander P., 1997, MNRAS, 286, 215

Kino, M. 2002, Ph.D. Thesis, Tohoku University

Kino, M., Takahara, F., & Kusunose, M. 2002, ApJ, 564, 97(KTK02)

Kirk, J. G. & Duffy, P. 1999, Journal of Physics G Nuclear Physics, 25, 163

Komissarov S. S., Falle S. A. E. G., 1998, MNRAS, 297, 1087

Krause M., 2003, A&A, 398, 113

Krolik, J. H. 1999, Active Galactic Nuclei, Princeton Series in Astrophysics, New Jersey

Kubo H. et al., 1998, ApJ, 504, 693

Landau, L. D., & Lifshitz, E. M. 1959, Fluid Mechanics, Pergamon Press, Oxford

Looney L. W., Hardcastle M. J., 2000, ApJ, 534, 172

Liu, R., Pooley, G., & Riley, J. M. 1992, MNRAS, 257, 545

Malkov, M. A. 1997, ApJ, 485, 638

Marti, J. M. A., Mueller, E., Font, J. A., Ibanez, J. M. A., & Marquina, A. 1997, ApJ, 479, 151

Mastichiadis A., Kirk J. G., 1997, A&A, 320, 19

Meisenheimer K., Yates M. G., Roeser H.-J., 1997, A&A, 325, 57

Norman M. L., Winkler K.-H. A., Smarr L., Smith M. D., 1982, A&A, 113, 285

Piran T., 1999, Phys. Rep., 314, 575

Rawlings S., Saunders R., 1991, Nature, 349, 138

Reynolds C. S., Fabian A. C., Celotti A., Rees M. J., 1996, MNRAS, 283, 873

Riley J. M., Pooley G. G., 1978, MNRAS, 183, 245

Tavecchio F., Maraschi L., Sambruna R. M., Urry C. M., 2000, ApJ, 544, L23

Sari R., Piran T., Narayan R., 1998, ApJL, 497, L17

Scheck L., Aloy M. A., Martí J. M., Gómez J. L., Müller E., 2002, MNRAS, 331, 615

Sikora M., Madejski G., 2000, ApJ, 534, 109

Smith M. D., Norman M. L., Winkler K.-H. A., Smarr L., 1985, MNRAS, 214, 67

Smith D. A., Wilson A. S., Arnaud K. A., Terashima Y., Young A. J., 2002, ApJ, 565, 195

Ueno S., Koyama K., Nishida M., Yamauchi S., Ward M. J., 1994, ApJ, 431, L1

Urry C. M., Padovani P., 1995, PASP, 107, 803

Wardle J. F. C., Aaron S. E., 1997, MNRAS, 286, 425

Wilson, A. S., Young, A. J., & Shopbell, P. L. 2000, ApJL, 544, L27

Table 1. Observables for the hot spots.

	Cygnus A	3C123
z	0.0562	0.2177
$F_{\text{syn}}(\text{erg s}^{-1} \text{ cm}^{-2})$	1×10^{-11}	1×10^{-12}
$F_{\text{SSC}}(\text{erg s}^{-1} \text{ cm}^{-2})$	5×10^{-13}	1×10^{-13}
$\nu_{\text{syn,o,max}}(\text{Hz})$	1×10^{11}	1×10^{11}
s	2.1	2.1
$R(\text{kpc})$	2.0	2.6

Notes: F_{syn} and F_{SSC} are the bolometric flux.

Table 2. Analytic estimate of physical parameters in the hot spots.

	Cygnus A	3C123
$B(\text{G})$	1×10^{-4}	8×10^{-5}
γ_{max}	3×10^4	3×10^4
γ_{br}	7×10^4	1×10^5
$q_e(\text{cm}^{-3} \text{s}^{-1})$	1×10^{-15}	7×10^{-16}
$U_{\text{rad}}/U_{3,\text{acc}}$	3×10^{-2}	2×10^{-2}
$U_{3,\text{acc}}/U_B$	5	14
cooling regime	weak	weak

Table 3. Physical parameters from SSC analysis for Cygnus A

Parameter	Cygnus A ($c_1 = 1$)	Cygnus A ($c_1 = 1/6$)
$B(\text{G})$	1.5×10^{-4}	1.6×10^{-4}
γ_{max}	1.5×10^4	3.0×10^4
$q_e(\text{cm}^{-3} \text{s}^{-1})$	2.0×10^{-15}	5.0×10^{-16}
$n_{3,\text{acc}}(\text{cm}^{-3})$	1.2×10^{-3}	1.4×10^{-3}
$\langle \gamma \rangle$	6	6
$F_{\text{syn}}(\text{erg s}^{-1} \text{ cm}^{-2})$	1.2×10^{-11}	1.3×10^{-11}
$F_{\text{SSC}}(\text{erg s}^{-1} \text{ cm}^{-2})$	4.7×10^{-13}	5.0×10^{-13}
$L_{\text{e,kin}}(\text{erg s}^{-1})$	2.9×10^{46}	3.3×10^{46}
$L_{\text{poy}}(\text{erg s}^{-1})$	4.3×10^{45}	4.8×10^{45}
$L_{\text{rad}}(\text{erg s}^{-1})$	1.7×10^{44}	1.8×10^{44}
$U_{\text{rad}}/U_{3,\text{acc}}$	5.9×10^{-3}	5.7×10^{-3}
$U_{3,\text{acc}}/U_B$	7	7

Notes: F_{syn} and F_{SSC} are the bolometric flux.

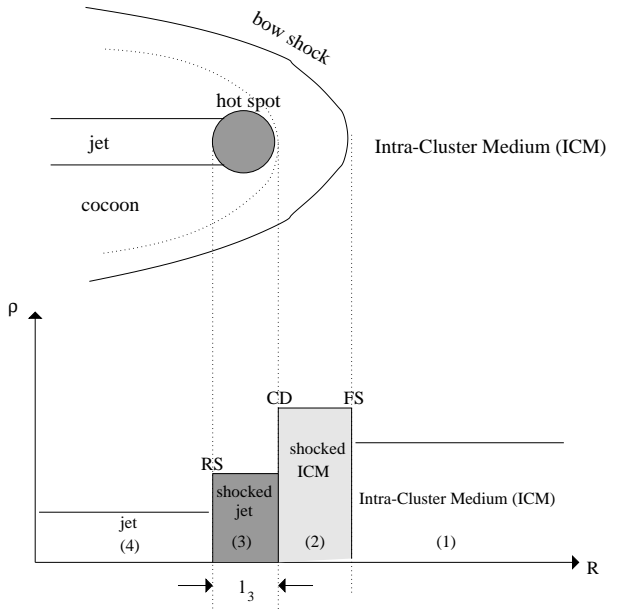
$\langle \gamma \rangle$ is the average Lorentz factor of non-thermal electrons and $\gamma_{\text{min}} = 1$.

Table 4. Physical parameters from SSC analysis for 3C123

Parameter	3C123($c_1 = 1$)	3C123($c_1 = 1/6$)
$B(\text{G})$	1.0×10^{-4}	1.45×10^{-4}
γ_{max}	5.0×10^4	8.0×10^4
$q_e(\text{cm}^{-3} \text{s}^{-1})$	2.1×10^{-15}	4.4×10^{-16}
$n_{3,\text{acc}}(\text{cm}^{-3})$	1.3×10^{-3}	1.6×10^{-3}
$\langle \gamma \rangle$	6.5	6.1
$F_{\text{syn}}(\text{erg s}^{-1} \text{ cm}^{-2})$	2.0×10^{-12}	2.4×10^{-12}
$F_{\text{SSC}}(\text{erg s}^{-1} \text{ cm}^{-2})$	2.8×10^{-13}	1.9×10^{-13}
$L_{\text{e,kin}}(\text{erg s}^{-1})$	5.8×10^{46}	6.6×10^{46}
$L_{\text{poy}}(\text{erg s}^{-1})$	3.2×10^{45}	6.8×10^{45}
$L_{\text{rad}}(\text{erg s}^{-1})$	5.1×10^{44}	5.7×10^{44}
$U_{\text{rad}}/U_{3,\text{acc}}$	8.9×10^{-3}	8.7×10^{-3}
$U_{3,\text{acc}}/U_B$	18	10

Notes: F_{syn} and F_{SSC} are the bolometric flux.

$\langle \gamma \rangle$ is the average Lorentz factor of non-thermal electrons and $\gamma_{\text{min}} = 1$.

**Figure 1.** Schematic view of shock dissipation at the head region of the relativistic jet. Upper panel shows the model geometry of shocks in an FR II radio galaxy. Lower panel shows the mass densities in each region. The reverse shocked region is identified as a hot spot. The forward shock is identified as a bow shock. The cocoon is composed of shocked jet material that has expanded sideways. The length l_3 is the longitudinal size of the hot spot.

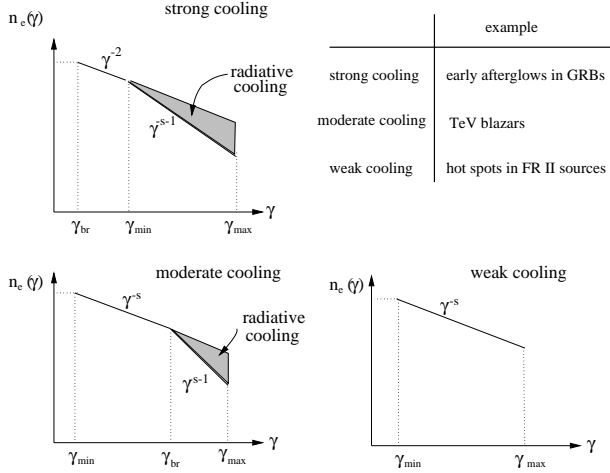


Figure 2. Cooling regimes for non-thermal electrons. For strong cooling (so-called *fast cooling* in Sari, Piran & Narayan 1998), injected electrons immediately lose their energy by radiative cooling. For moderate cooling (*slow cooling*), at high Lorentz factors, radiative cooling decreases the number density of electrons and leads to a break in the spectrum. For weak cooling, the cooling time scale is sufficiently long and the radiative cooling does not change the injected electron spectrum. An example of specific objects in each regime is also shown.

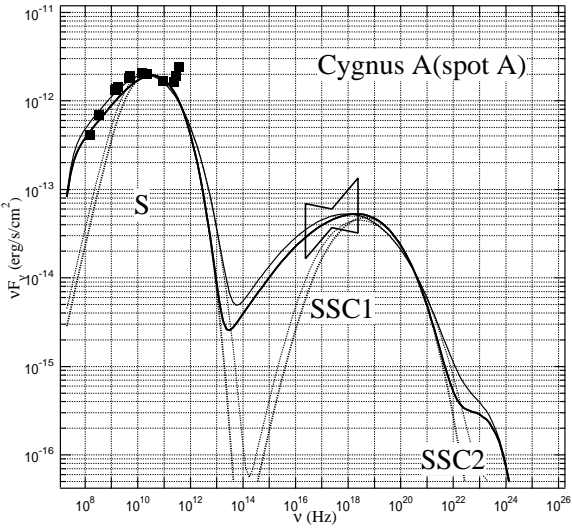


Figure 3. One-zone model spectrum for the emission from the hot spot A of Cygnus A. The observed data are taken from those compiled by Wilson, Young, & Shopbell (2000). The thick solid line shows the best fit spectrum in the case of $\gamma_{\min} = 1$ and $c_1 = 1$. The thick dotted line shows the case of $\gamma_{\min} = 2000$ and $c_1 = 1$, which is not acceptable to fit the observed one. The thin solid line shows the case of $\gamma_{\min} = 1$ and $c_1 = 1/6$. The thin dotted line shows the case of $\gamma_{\min} = 2000$ and $c_1 = 1/6$ can be also ruled out.

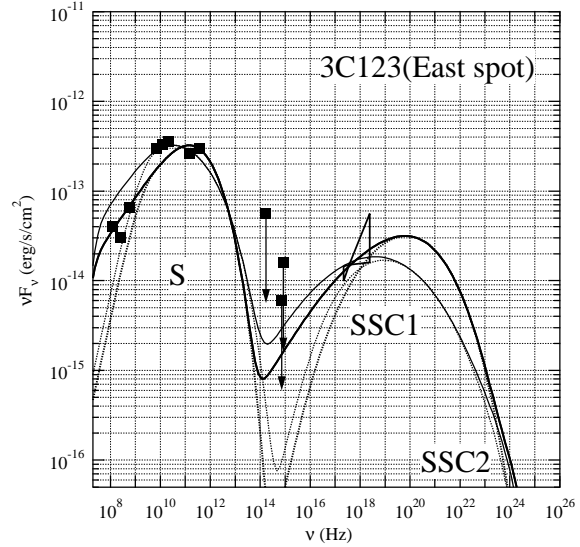


Figure 4. One-zone model spectrum for the emission from the hot spot in 3C 123. The observed data are taken from those compiled by Hardcastle, Birkinshaw, & Worrall (2001). The thick solid line shows the best fit spectrum. The thick dotted line shows the case of $\gamma_{\min} = 2000$, which is not acceptable. The thin solid line shows the case of $\gamma_{\min} = 1$ and $c_1 = 1/6$ which overestimate the observed radio flux. The thin dotted line shows the case of $\gamma_{\min} = 2000$ and $c_1 = 1/6$ which explains the radio band while it tends to underestimate the X-ray band.

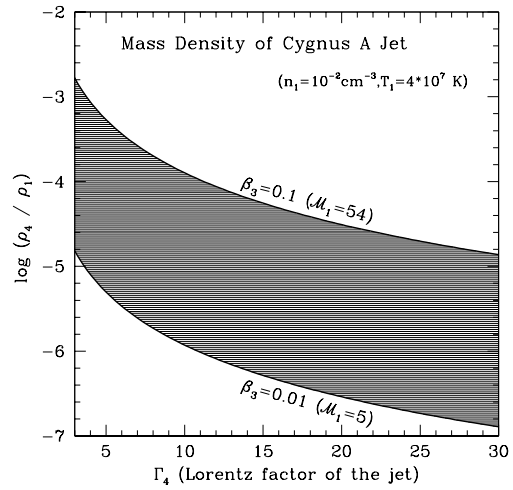


Figure 5. The rest mass density ratio of the AGN jet to the hot ICM in the case of Cygnus A (see also Figure 1). Proton number density and temperature in the ICM (region 1) are taken from Arnaud et al. (1984).

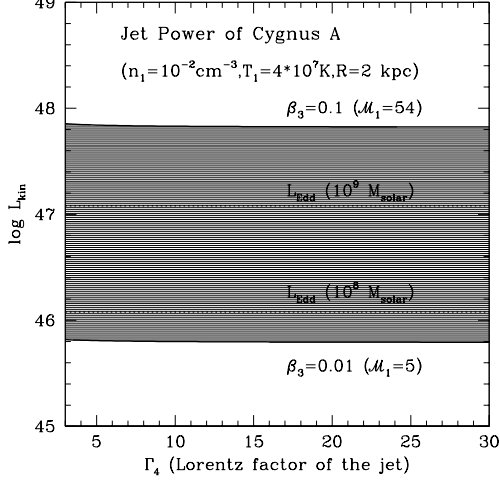


Figure 6. The total kinetic power of Cygnus A jet. Shadowed region corresponds to the allowable range of $0.01 < \beta_3 < 0.1$. To generate higher hot spot speed β_3 , higher μ_4 is required. We show the Eddington luminosity (dotted lines) for comparison for several values of black hole mass.

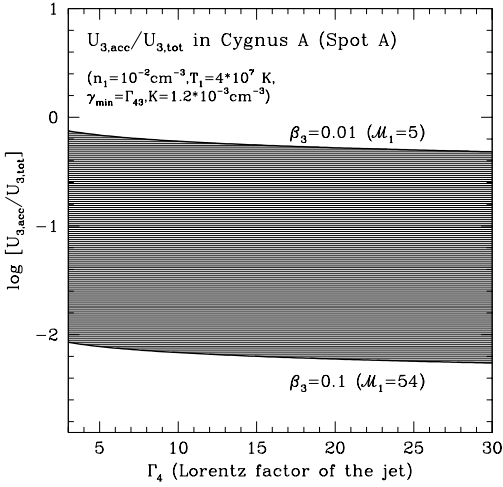


Figure 7. The energy density ratio of accelerated electrons to the total particles. Solid lines represent the ratio in the case of $\beta_3 = 0.1$ and $\beta_3 = 0.01$, respectively.

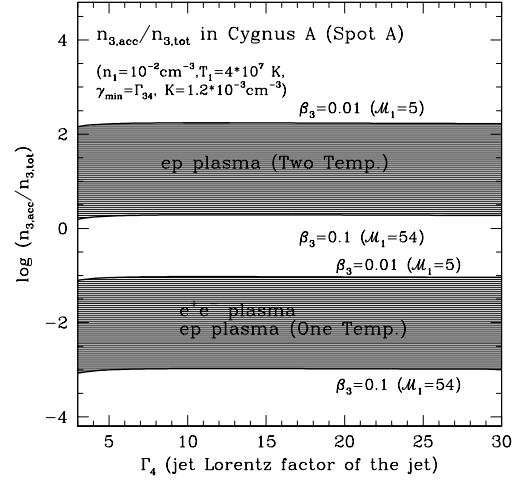


Figure 8. The number density ratio of $n_{3,acc}/n_{3,tot}$. The upper shadowed region corresponds to the range of $0.01 < \beta_3 < 0.1$ for pure ep plasma with two temperature (Case II). This region is ruled out simply because the value $n_{3,acc}/n_{3,tot} > 1$ is forbidden by definition. The lower shadowed region corresponds to the range of $0.01 < \beta_3 < 0.1$ for purely e^\pm plasma (Case I) and pure ep plasma with one temperature (Case III).

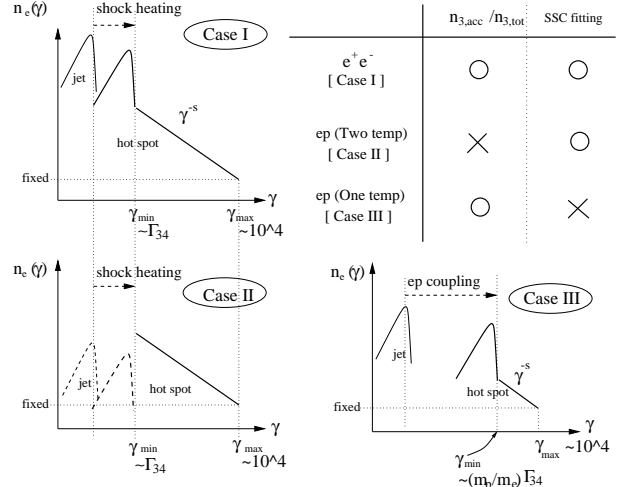


Figure 9. The summary of plasma composition diagnosis and sketches of the electron energy spectra in Case I, II, and III. Thick solid line in each panel shows the spectra in the hot spot. Thin solid line in each panel shows the cold jet. Dashed lines in Case II (in left lower panel) imply that the number density of non-thermal electrons exceeds that of total particles and that this case is ruled out. The normalization of non-thermal electron number density in the hot spot is fixed by SSC model fitting.